# Boosting the surface conduction in a topological insulator

**Mathieu Taupin** ( ✉ taupin@ifp.tuwien.ac.at )
Vienna University of Technology

**Gaku Eguchi**
Institute of Solid State Physics, Vienna University of Technology

**Monika Budnowski**
Vienna University of Technology

**Andreas Steiger-Thirsfeld**
Vienna University of Technology

**Yukiaki Ishida**
ISSP, University of Tokyo    https://orcid.org/0000-0002-0980-7041

**Kenta Kuroda**
University of Tokyo    https://orcid.org/0000-0002-0151-0876

**Shik Shin**
University of Tokyo    https://orcid.org/0000-0002-2505-9362

**Akio Kimura**
Graduate School of Science, Hiroshima University    https://orcid.org/0000-0002-1501-3918

**Silke Paschen**
TU Wien    https://orcid.org/0000-0002-3796-0713

---

**Article**

---

# Boosting the surface conduction in a topological insulator

M. Taupin,[1, *] G. Eguchi,[1, *] M. Budnowski,[1] A. Steiger-Thirsfeld,[2]

Y. Ishida,[3] K. Kuroda,[3, 4] S. Shin,[3] A. Kimura,[4] and S. Paschen[1]

[1]*Institute of Solid State Physics, TU Wien,*

*Wiedner Hauptstr. 8-10, 1040 Vienna, Austria*

[2]*USTEM, TU Wien, Wiedner Hauptstr. 8-10, 1040 Vienna, Austria*

[3]*ISSP, The University of Tokyo, Kashiwa, Chiba 277-8581, Japan*

[4]*Graduate School of Advanced Science and Engineering, Hiroshima University,*

*1-3-1 Kagamiyama, Higashi-Hiroshima 739-8526, Japan*

(Dated: August 5, 2021)

## Abstract

The protected surface conduction of topological insulators is in high demand for the next generation of electronic devices. What is needed to move forward are robust settings where topological surface currents can be controlled by simple means, ideally by the application of external stimuli. Surprisingly, this direction is only little explored and the role of topological states in such processes has remained obscure. In this work we demonstrate that we can boost the surface conduction of a topological insulator by light and/or electric field. This happens in a fully controlled way, and the additional Dirac carriers exhibit ultra-long live times. We provide a comprehensive understanding—carriers injection from the bulk to the surface states across an intrinsic Schottky barrier—and expect this mechanism to be at play in a broad range of materials and experimental settings.

The past decade has seen a wealth of studies on topological insulators[1–3], motivated at least in part by the potential of these materials for the next generation of electronic devices. Despite massive efforts, important questions remain to be answered. For instance, a number of topological insulators have shown anomalous responses when exposed to light[4–9], most notably slow and non-exponential relaxation behaviour, that hints at the tunability of the Dirac surface states with illumination. The lack of consensus of the microscopic mechanism impedes progress. Slow relaxation behaviours have also been observed in experiments without irradiation[10,11]. The salient feature of all these studies[4–11]—persistence with non-exponential relaxation—suggests a common underlying origin. Our work provides an understanding of these effects. We demonstrate that under external excitation (such as thermal radiation, light illumination, and current driving), excited electrons will migrate to the surface states and remain there "permanently" due to the intrinsic Schottky barrier and space-charge separation between the surface and bulk carriers. This leads to a significant boost of the surface conduction, which can be adjusted by the amplitude of the external excitation. We find striking similarities between our results and previous spectroscopic studies[12–18] and propose a mechanism that should hold for any topological insulator. This new understanding opens new routes to further fundamental studies and may pave the way towards applications of robust bulk 3D topological insulators.

## RESULTS

**The material.** Our electrical transport study was performed on the bulk topological insulator $Tl_{1-x}Bi_{1+x}Se_{2-\delta}$[19–23] (Fig. 1**a**). This compound features an isolated surface Dirac point situated in the band gap of the bulk states, the absence of trivial surface states as observed by angle resolved photoemission spectroscopy (ARPES), and a great tunability of the Fermi level by changing the off-stoichiometry via the variation of $x$[24,25]. This is seen in ARPES as an energy shift of the Fermi level with $x$ and in electrical resistivity measurements as orders of magnitude variation of the low-temperature resistivity with $x$ (Fig. 1**b** and **c**). The presence of high mobility electrons (the surface Dirac electrons) and low mobility (bulk) holes is evidenced from a two-carrier analysis[26,27] (Extended Data 1).

In the temperature-dependent electrical resistivity curves of samples with $x < 0.064$, we observe a semiconducting behaviour with an anomaly at a characteristic temperature $T^* \approx 40$ K. This anomaly is also seen in the dc-susceptibility but not in the specific heat (Extended Data 2), indicating that it is not a bulk effect but should instead be attributed to surface states. In what follows we focus on the bulk-insulating compound $x = 0.025$. By lowering the temperature, its current-voltage characteristics evolve from a regular quasi-linear (ohmic) to a Schottky-like behaviour. This is attributed to the presence of a Schottky barrier between the Dirac surface states and the gapped bulk states due to band bending[28,29], as sketched in Fig. 1**d** (see also Supplementary Information). Below $T^*$, in addition we observe the appearance of switching behaviour and a memory effect. This anomalous behaviour is discussed later and we first describe the photoresponse of the electrical resistivity.

**Radiation effects.** Various kinds of (modest) radiation profoundly modify the transport behaviour below $T^*$. In a first set of experiments, we measured the electrical resistivity of the bulk-insulating sample during cooling to 2 K, expose it there to illumination from a near-infrared light emitting diode (NIR LED), then switch off the LED and measure the electrical resistivity during warming (Fig.2**a**). The orange and green curves are for two such runs, with a shorter and a longer illumination time, respectively, the latter being long enough to reach a steady state (i.e., even longer irradiation does not lead to a further resistance change). Compared to the measurement without illumination, a strong decrease of the low-temperature electrical resistivity is observed, up to an order of magnitude at 2 K, corresponding to a large positive photoconductivity, with the size of the effect being controlled by the illumination duration.

3

Intriguingly, also black-body radiation affects the resistivity, which we noticed when performing an experiment without a radiation shield (see Methods). We present two experiments, one with a shortened radiation shield (leading to black-body radiation from temperatures only slightly above the sample temperature) and one without a shield (leading to black-body radiation from room temperature), as shown in Fig. 2**a** and Extended Data 4**a**. In both cases, the sample was held at 2 K under these shielding conditions until a steady state was reached, and then measured during warming. The experiment with incomplete shielding results in a much weaker resistivity reduction than the experiment without a shield. On the other hand we see that the data from the experiments with (steady state) black-body radiation from room temperature and NIR radiation from the LED almost collapse.

Before proceeding, we note on several points. Firstly, the sensitivity to even spurious thermal radiation explains the anomalies at $T^*$ in the resistivity curves taken without intentional illumination (see Fig. 1**c**). Secondly, after illumination, the initial high resistance state is recovered by heating the sample above $T^*$. This excludes surface pollution[28,30] and sample ageing effects[31] as origins because they are not reversible with temperature. And thirdly, the effect is seen after the illumination is switched off. Thus, the photoexcited carriers have a lifetime that is, at least, long on the time scale of the resistivity measurement.

To explore the relaxation behaviour further, we measured the electrical resistivity at several fixed temperatures as function of time, both during illumination with the NIR LED ($0 < t < 7200$ s) and after switching it off ($t > 7200$ s, Fig. 2**c**). At high temperatures, the relaxation is fast on the time scales of our measurements (about 1 s) but with decreasing temperature an increasingly slow relaxation is observed (spurious heating effects are discussed in Extended Data 5). Most striking is the effect that when switching the LED off after having reached the equilibrium state at 2 K, the resistivity barely evolves on the time scale of our experiment (see lowest temperature curve in Fig. 2**c**). This is the phenomenon of persistent photoconductivity.

We also analyse the time dependence quantitatively. The relaxation after switching the LED off follows a stretched-exponential relaxation[32], $R \propto \exp\left[-(\frac{t}{\tau})^n\right]$ (with $n < 1$), as shown by the black lines in Fig. 2**c** (with the condition $R_{t\to\infty} = R_{t<0}$ during relaxation). The temperature dependence of the relaxation time $\tau$ is shown in Fig. 2**d**. It increases by almost 9 orders of magnitude as temperature is only slightly reduced, from 35 to 20 K, before saturating at lower temperatures. Above 20 K, this temperature dependence can be approximated by a thermal activation law, $\ln(\tau) \propto E_B/k_B T$, with $E_B \approx 82$ meV interpreted as the height of a Schottky barrier.

4

From this dependence we derive that, below 20 K, a relaxation of the resistivity to 90% of its initial value before irradiation would take hundreds of years—persistence par excellence (see Extended Data 5).

**Current effects.** Next we show that the surface conductivity can also be tuned using electrical currents. Applying a large current at low temperatures leads to a controlled and permanent decrease of the resistivity which, analogous to the illumination experiments, is measured upon warming, after reducing the large tuning current to a small measurement current of 10 $\mu$A to exclude overheating (Fig. 2**b**). Again, the effect is reversible by heating the sample above $T^*$.

This current-induced decrease of the resistivity below $T^*$ is visible in the current-voltage characteristics as a memory effect. In the 2 K isotherm (Fig. 1**e**), a hysteresis is observed between the increasing-current curve (from 0 to 50 mA) and the decreasing-current curve (from 50 mA back to 0) but, interestingly, not between the subsequent up and down sweeps with negative applied current. The hysteresis can thus be attributed to the current-induced switching from the initial high-resistance state (black line in Fig. 2**b**) to the low-resistance state (purple triangles). Once the sample has switched, it remains in the low-resistance state until it is heated above $T^*$. Thus, no hysteresis appears under negative currents, and not under positive currents in a second loop either. The characteristic time of the current-induced resistivity change is much faster than that of the illumination-induced process; in fact, it is smaller than the typical time scale of our measurements (about 1 s) and could thus not be resolved.

**Interpretation.** How can we understand the salient features observed in all these experiments in a consistent way? From the similarities between the light-induced and electrical current-driven reduction of the resistivity, a common mechanism is expected and therefore both purely optical[4,6] and purely electric-field-induced effects[10,33,34] are excluded. In addition, we observe essentially the same behaviour in samples with different off-stoichiometry/doping level, in microfabricated samples (see below), and in a bulk metallic sample (when the Fermi level is in the bulk conduction band), see Extended Data 6. This indicates that the effects are robust against changes of the Fermi level, impurity concentrations, and eventual surface potential fluctuations, therefore discarding trapped charges in the band gap as origin[35–37].

We first address the effects induced by the NIR radiation, i.e., the large positive and persistent photoconductivity with streched-exponential relaxation. NIR light penetrates $0.16 - 1\,\mu$m into the sample—much deeper than the depletion depth $W$ (around 15 nm, see Methods)—and has sufficient energy ($\approx 1.25$ eV) to excite carriers across the bulk bandgap ($\geq 0.3$ eV[23]). Thus, we propose

that electrons, photoexcited across the bulk bandgap, migrate to the surface due to the downward band bending associated with a Schottky barrier, and populate the Dirac surface states (as sketched in Fig. 2**e** top). This creates a surface charge accumulation with space-charge separation[38,39] between the Dirac electrons and the bulk holes. By populating the Dirac states, the barrier height $E_B$ and, as a consequence, the depletion width $W$ (see Eq. 1 in the Methods) decrease. This model is supported by Hall effect experiments. They reveal a pronounced illumination-induced change of the Hall coefficient below $T^*$ (Extended Data 1) which, in an extended two-carrier analysis, is associated with an 8-fold increase of the surface carrier concentration, or equivalently by an increase of the contribution of the surface states to the total conductivity by a factor 2.4 (see Supplementary Information). The stretched-exponential decay is understood as follows: the photoexcited Dirac electrons on the surface are separated from the photoexcited holes in the bulk by the Schottky barrier. At low temperatures, the recombination process is dominated by tunnelling across the depleted area (as sketched in Fig. 2**e** bottom). The barrier height $E_B$ and depletion width $W$ increase as the Dirac states are depopulated. As a consequence, the tunnelling rate decreases with time during relaxation, compatible with the stretched-exponential decay.

We now turn to the sensitivity to spurious black-body radiation. The power density from a black body at 300 K is centered at 155 meV (8 $\mu$m) with a significant part of the distribution above 300 meV, which is large enough to excite carriers across the energy gap. The steady-state photo-conductivity from this radiation is almost identical to the one from the much higher energy NIR LED (see Fig. 2**a**). This shows that, as long as the radiation has sufficient energy to excite carriers across the energy gap, a unique steady-state conductivity is reached. This provides further support for the conductivity in the irradiated state being dominated by surface conduction because the different energy ranges of the two types of radiations imply different penetration depths into the sample. If this resistivity reduction were due to (metastable) bulk carriers, different portions of the bulk sample would contribute and thus different saturation resistivities would be observed. By contrast, black-body radiation from much lower temperature as expected from the shortened radiation shield has insufficient energy to excite carriers across the bulk gap. However, because bulk-insulating $Tl_{1-x}Bi_{1+x}Se_{2-\delta}$ is slightly off-stoichiometric, there may be shallow in-gap states with trapped carriers, and these might be photoexcited to the bulk conduction (or valence) band. This can explain the weaker resistivity reduction of the curve with partial shielding (red curve in Fig. 2**a**).

Next we discuss the electrical current-driven effect. As shown above, there is a current thresh-

6

old (between 10 and 15 mA, Fig. 1**e**, see also Extended Data. 3) for low-temperature resistance switching to occur. For currents (and corresponding electrical fields) above this threshold, the bulk conduction band is partially populated by electrons via electric field injection[40] (see Supplementary Information). At low temperatures, these electrons then increase the "current-induced conductivity", analogous to the photoconductivity under irradiation.

**Microfabricated samples.** We now present photocontrol studies on micrometric samples, fabricated with the focused-ion beam (FIB) cutting technique[41] from a bulk sample ($x = 0.025$) (Fig. 3**a**, see also Methods). The temperature-dependent resistances of two such samples again show a pronounced drop below about 40 K when illuminated and the time dependence upon illumination again follows stretched-exponential behaviour (Fig. 3**b** and **c**). Both this qualitative similarity to the results on the bulk sample and two quantitative differences, reported next, lend further support to our interpretation, and confirm that the surface states are directly involved. Firstly, during illumination, the saturation resistance is reached in only a few minutes instead of a few hours, which we attribute to the light penetration depth being similar to or larger than the thickness of the sample ($0.16 - 1\,\mu$m and $0.3\,\mu$m, respectively), and thus the irradiation hitting the entire volume of the sample. Secondly, the resistance under illumination is lower at low temperature than it is at room temperature (ratio $R/R_{300\,\mathrm{K}} < 1$), which we understand as caused by a much larger relative contribution of the surface conduction in the samples. Our results demonstrate the robustness of the photocontrol of Dirac surface conduction against microfabrication, thus paving the way for device applications.

**ARPES.** Finally we studied the Dirac surface states with time-resolved ARPES (tr-ARPES) experiments. In the bulk-insulating sample ($x = 0.025$), after pumping, a shift of the (quasi-)Fermi level by 93 meV is observed and persists for at least $4\,\mu$s (Fig. 4**a**, **c** and Extended Data 7**a**, **c**). This shift is composed of an actual shift of the Fermi level on the surface by $\delta_E = 28$ meV—caused by the filling of the Dirac states upon pumping (Fig. 4**f-h**)—and of a shift by $\Delta_E = 65$ meV caused by a surface photovoltage due to a relaxation of the band bending (Fig. 4**g**). To visualize the charge accumulation at the surface more directly, we subtract the spectrum without pump but shifted by 65 meV (Fig. 4**b**) from the spectrum taken $4\,\mu$s after the pump (Fig. 4**c**). The difference spectrum (Fig. 4**d**) as well as the difference of the angle-integrated intensity (Fig. 4**e**) clearly reveal extra charge corresponding to a Fermi level shift of 28 meV. No such "persistent" shift of the Fermi level is detected in the bulk-metallic sample (Extended Data 7**b**, **d**). In addition, very different relaxation times of the excited states between both samples are found (Extended Data 7**e**). Only

7

if the Fermi level is situated inside the bulk band gap, we observe a slow ($\geq 4\,\mu$s) relaxation, similar to that observed in other topological insulators[13–18]. Our accompanying transport study on the same material allows us to relate this "more-than-$4\,\mu$s-long" relaxation to an ultraslow "more-than-hour-long" relaxation. We conjecture that the underlying mechanism is the same and that, thus, also the tr-ARPES pump induces a state of persistent topological surface conduction in bulk insulating $Tl_{1-x}Bi_{1+x}Se_{2-\delta}$ ($x = 0.025$).


**DISCUSSION**


We have demonstrated in this work that topological surface states can be permanently populated by carriers, enhancing the conductivity of the surface states. This is achieved using simple external stimuli, i.e. illumination and electrical current. The mechanism proposed here—space-charge separation between the surface and bulk carriers—is relevant for any topological insulator. It is surprising that these effects have remained largely unnoticed and not understood[4–11]. Possibly, the anomaly in transport observed in Cd-doped $Bi_2Se_3$[42] and Sn-doped $Bi_{1.1}Sb_{0.9}Te_2S$[43] are analogous to what we observe here, just as the large difference between (dc-)resistivity and optical conductivity (therefore after irradiation) in $BiSbTeSe_2$[44] and the persistence of the voltage-induced superconductivity in $Bi_2Se_3$[45].

We expect our work to have broad impact. Firstly, our demonstration of the extreme sensitivity of the surface states to even weak irradiation will raise awareness that extra care needs to be taken in order to probe the ground state of a topological insulator, particularly in spectroscopic experiments where shielding is difficult. Secondly, we have put forward experiments with readily accessible "pumping"—weak light/radiation or electrical current—which lend themselves for experiments also on other samples in many laboratories worldwide, as well as for implementation in experiments beyond transport. An interesting candidate for such future studies is the putative topological Kondo insulator $SmB_6$[12]. Thirdly, because of the persistence of the surface conduction, the "pump" can be switched off after the surface charge is generated. This will avoid any interferences with it both in fundamental studies and future device applications. And finally, the control does not rely on the presence of defect or impurity states and is even robust against rather harsh microstructuring techniques, ensuring reliability.

8

215    * These authors have contributed equally.

216   1. Hasan, M. Z. & Kane, C. L. Colloquium: Topological insulators. *Rev. Mod. Phys.* **82**, 3045 (2010).

217   2. Qi, X.-L. & Zhang, S.-C. Topological insulators and superconductors. *Rev. Mod. Phys.* **83**, 1057
218      (2011).

219   3. Wehling, T., Black-Schaffer, A. & Balatsky, A. Dirac materials. *Adv. Phys.* **63**, 1 (2014).

220   4. Yeats, A. L. *et al.* Persistent optical gating of a topological insulator. *Science Adv.* **1**, e1500640 (2015).

221   5. Zheng, K. *et al.* Optoelectronic characteristics of a near infrared light photodetector based on a topo-
222      logical insulator $Sb_2Te_3$ film. *J. Mater. Chem. C.* **3**, 9154 (2015).

223   6. Pirralho, M. J. P. *et al.* Investigation of photoconductive effect on $Bi_2Te_3$ epitaxial film. *Appl. Phys.*
224      *Lett.* **114**, 112101 (2019).

225   7. Kang, T. T. & Chen, P. P. $Bi_2Te_3$ photoconductive detector under weak light. *J. Appl. Phys.* **126**,
226      083103 (2019).

227   8. Hou, Y., Xiao, R., Li, S., Wang, L. & Yu, D. Non-local chemical potential modulation in topological
228      insulators via electric field driven trapped charge migration. *ArXiv e-prints* (2020). 2004.01847.

229   9. Xie, F. *et al.* Reversible engineering of topological insulator surface state conductivity through optical
230      excitation. *Nanotechnol.* **32**, 17LT01 (2021).

231 10. Tian, J., Hong, S., Miotkowski, I., Datta, S. & Chen, Y. P. Observation of current-induced, long-lived
232      persistent spin polarization in a topological insulator: A rechargeable spin battery. *Science Adv.* **3**,
233      e1602531 (2017).

234 11. Li, M. *et al.* Electron delocalization and relaxation behavior in Cu-doped $Bi_2Se_3$ films. *Phys. Rev. B*
235      **96**, 075152 (2017).

236 12. Ishida, Y. *et al.* Emergent photovoltage on $SmB_6$ surface upon bulk-gap evolution revealed by pump-
237      and-probe photoemission spectroscopy. *Sci. Rep.* **5**, 8160 (2015).

238 13. Neupane, M. *et al.* Gigantic Surface Lifetime of an Intrinsic Topological Insulator. *Phys. Rev. Lett.*
239      **115**, 116801 (2015).

240 14. Sumida, K. *et al.* Prolonged duration of nonequilibrated Dirac fermions in neutral topological insula-
241      tors. *Sci. Rep.* **7**, 14080 (2017).

242 15. Yoshikawa, T. *et al.* Enhanced photovoltage on the surface of topological insulator via optical aging.
243      *Appl. Phys. Lett.* **112**, 192104 (2018).

244  16. Papalazarou, E. *et al.* Unraveling the Dirac fermion dynamics of the bulk-insulating topological system

245       $Bi_2Te_2Se$. *Phys. Rev. Mater.* **2**, 104202 (2018).

246  17. Yoshikawa, T. *et al.* Bidirectional surface photovoltage on a topological insulator. *Phys. Rev. B* **100**,

247       165311 (2019).

248  18. Ciocys, S. *et al.* Manipulating long-lived topological surface photovoltage in bulk-insulating topologi-

249       cal insulators $Bi_2Se_3$ and $Bi_2Te_3$. *npj Quantum Mater.* **5**, 16 (2020).

250  19. Eremeev, S. V., Koroteev, Y. M. & Chulkov, E. V. Ternary thallium-based semimetal chalcogenides

251       Tl-V-VI2 as a new class of three-dimensional topological insulators. *JETP Lett.* **91**, 594 (2010).

252  20. Lin, H. *et al.* Single-Dirac-Cone Topological Surface States in the $TlBiSe_2$ Class of Topological

253       Semiconductors. *Phys. Rev. Lett.* **105**, 036404 (2010).

254  21. Yan, B. *et al.* Theoretical prediction of topological insulators in thallium-based III-V-VI 2 ternary

255       chalcogenides. *EPL (Europhys. Lett.)* **90**, 37002 (2010).

256  22. Sato, T. *et al.* Direct Evidence for the Dirac-Cone Topological Surface States in the Ternary Chalco-

257       genide $TlBiSe_2$. *Phys. Rev. Lett.* **105**, 136802 (2010).

258  23. Kuroda, K. *et al.* Experimental Realization of a Three-Dimensional Topological Insulator Phase in

259       Ternary Chalcogenide $TlBiSe_2$. *Phys. Rev. Lett.* **105**, 146801 (2010).

260  24. Kuroda, K. *et al.* Tunable spin current due to bulk insulating property in the topological insulator

261       $Tl_{1-x}Bi_{1+x}Se_{2-\delta}$. *Phys. Rev. B* **91**, 205306 (2015).

262  25. Eguchi, G., Kuroda, K., Shirai, K., Kimura, A. & Shiraishi, M. Surface Shubnikov-de Haas oscillations

263       and nonzero Berry phases of the topological hole conduction in $Tl_{1-x}Bi_{1+x}Se_2$. *Phys. Rev. B* **90**,

264       201307 (2014).

265  26. Eguchi, G. *et al.* Precise determination of two-carrier transport properties in the topological insulator

266       $TlBiSe_2$. *Phys. Rev. B* **91**, 235117 (2015).

267  27. Eguchi, G. & Paschen, S. Robust scheme for magnetotransport analysis in topological insulators. *Phys.*

268       *Rev. B* **99**, 165128 (2019).

269  28. Hsieh, D. *et al.* A tunable topological insulator in the spin helical Dirac transport regime. *Nature* **460**,

270       1101 (2009).

271  29. Checkelsky, J. G., Hor, Y. S., Cava, R. J. & Ong, N. P. Bulk Band Gap and Surface State Conduction

272       Observed in Voltage-Tuned Crystals of the Topological Insulator $Bi_2Se_3$. *Phys. Rev. Lett.* **106**, 196801

273       (2011).

274  30. Frantzeskakis, E. *et al.* Trigger of the Ubiquitous Surface Band Bending in 3D Topological Insulators.

275    *Phys. Rev. X* **7**, 041041 (2017).

31. Taskin, A. A., Ren, Z., Sasaki, S., Segawa, K. & Ando, Y. Observation of Dirac Holes and Electrons in a Topological Insulator. *Phys. Rev. Lett.* **107**, 016801 (2011).

32. Phillips, J. C. Stretched exponential relaxation in molecular and electronic glasses. *Rep. on Prog. in Phys.* **59**, 1133 (1996).

33. Fu, Y.-S. *et al.* Memory Effect in a Topological Surface State of $Bi_2Te_2Se$. *ACS Nano* **7**, 4105 (2013).

34. Kalkan, N. & Bas, H. Electrical and Switching Properties of $TlBiSe_2$ Chalcogenide Compounds. *J. of Electron. Mater.* **44**, 4387 (2015).

35. Lang, D. V. & Logan, R. A. Large-Lattice-Relaxation Model for Persistent Photoconductivity in Compound Semiconductors. *Phys. Rev. Lett.* **39**, 635 (1977).

36. Zukotynski, S., Ng, P. C. H. & Pindor, A. J. Persistent photoconductivity in Si-doped $Al_xGa_{1-x}As$. *Phys. Rev. Lett.* **59**, 2810 (1987).

37. Scalvi, L. V. A. & Bueno, C. F Transient decay of photoinduced current in semiconductors and heterostructures. *J. Phys. D: Appl. Phys.* **53**, 033001 (2020).

38. Queisser, H. J. Nonexponential Relaxation of Conductance near Semiconductor Interfaces. *Phys. Rev. Lett.* **54**, 234 (1985).

39. Queisser, H. J. & Theodorou, D. E. Decay kinetics of persistent photoconductivity in semiconductors. *Phys. Rev. B* **33**, 4027 (1986).

40. Sze, S. M. & Kwok, K. N. *Physics of semiconductor devices* (Hoboken, N.J: Wiley-Interscience, 2007).

41. Friedensen, S., Mlack, J. T. & Drndic, M. Materials analysis and focused ion beam nanofabrication of topological insulator $Bi_2Se_3$. *Sci. Rep.* **7**, 13466 (2017).

42. Ren, Z., Taskin, A. A., Sasaki, S., Segawa, K. & Ando, Y. Observations of two-dimensional quantum oscillations and ambipolar transport in the topological insulator $Bi_2Se_3$ achieved by Cd doping. *Phys. Rev. B* **84**, 075316 (2011).

43. Kushwaha, S. K. *et al.* Sn-doped $Bi_{1.1}Sb_{0.9}Te_2S$ bulk crystal topological insulator with excellent properties. *Nat. Commun.* **7**, 11456 (2016).

44. Borgwardt, N. *et al.* Self-organized charge puddles in a three-dimensional topological material. *Phys. Rev. B* **93**, 245149 (2016).

45. Le, T. *et al.* Erasable superconductivity in topological insulator $Bi_2Se_3$ induced by voltage pulse. *Adv. Quantum Technol.* **-**, 2100067 (2021).
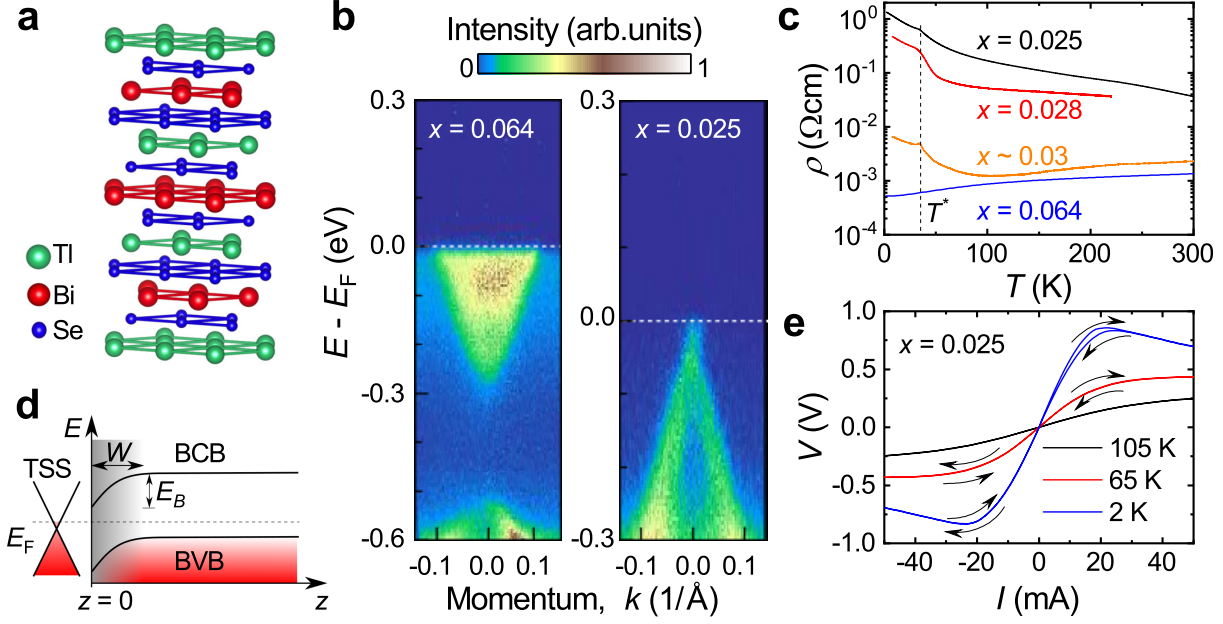
FIG. 1. **Characterization of $Tl_{1-x}Bi_{1+x}Se_{2-\delta}$ single crystals. a**: Crystal structure forming Tl-Se-Bi-Se quadruple layers. **b**: ARPES measurement around the $\bar{\Gamma}$ point of the bulk-metallic ($x = 0.064$, left) and bulk-insulating sample ($x = 0.025$, right) at 7 K. **c**: Temperature dependence of the electrical resistivity for samples with different off-stochiometry $x$. An anomaly is visible at $T^* \simeq 40$ K, independent of $x$. **d**: Sketch of the energy $E$ vs distance from surface $z$ without external stimulus, when the Fermi energy $E_F$ lies in the bulk band gap, showing the formation of a Schottky barrier. $W$ and $E_B$ are the depletion region and barrier height, TSS the topological surface states, and BVB and BCB the bulk valence band the bulk conduction band, respectively. **e**: Current-voltage characteristics of the sample with $x = 0.025$ at selected temperatures without illumination, showing deviations from Ohm's law due to the presence of the Schottky barrier and the development of switching and memory effects below $T^*$. The arrows indicate the measurement sequence: $0 \rightarrow 50$ mA $\rightarrow -50$ mA$\rightarrow 0$.

12
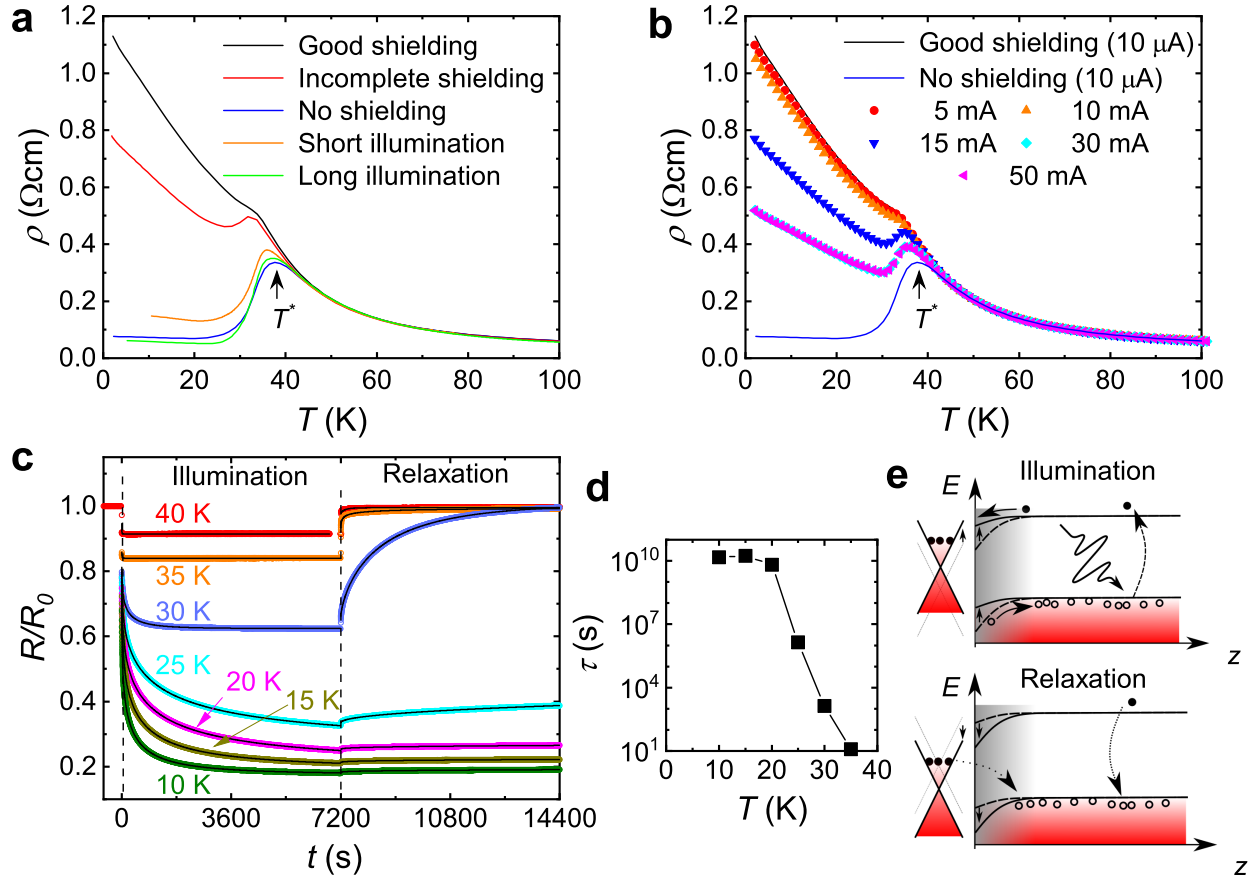
FIG. 2. **Tuning the surface conductivity of $Tl_{1-x}Bi_{1+x}Se_{2-\delta}$ ($x = 0.025$) in transport. a**: Photocontrol of the resistivity under different conditions. The poorer the thermal shielding (black $\rightarrow$ red $\rightarrow$ blue), the stronger the resistivity suppression below $T^*$ (see also Extended Data 4). Intentional illumination with a NIR source (orange, green) was applied with two different exposure times at 2 K, and switched off just before the measurements were performed upon warming. All measurements were done with an excitation current of $10\,\mu$A. **b**: Current-control of the resistivity, with different currents applied at 2 K before the measurements, which were then performed with $10\,\mu$A upon warming. All current-controlled measurements were performed under good thermal shielding. The blue and black curves are reproduced from **a** for comparison. **c**: Time dependence of the normalized resistance upon illumination below 40 K. The illumination is on between $t = 0$ and 7200 s, and then is switched off. The black solid lines are fits using a stretched-exponential (see text). **d**: Relaxation time $\tau$ as function of temperature, reaching 317 years at 10 K. **e**: Energy vs distance from surface diagrams, sketching the illumination and relaxation process. Under illumination, photoexcited electrons and holes are generated in the bulk, and migrate to the surface and bulk states, respectively, due to the downward band-bending. This leads to surface charge accumulation and space-charge separation, modifying thus the band-bending and shifting the Dirac cone accordingly. After turning off the illumination, the excited Dirac electrons recombine with the excited bulk holes, which at low temperatures can only occur via tunneling.
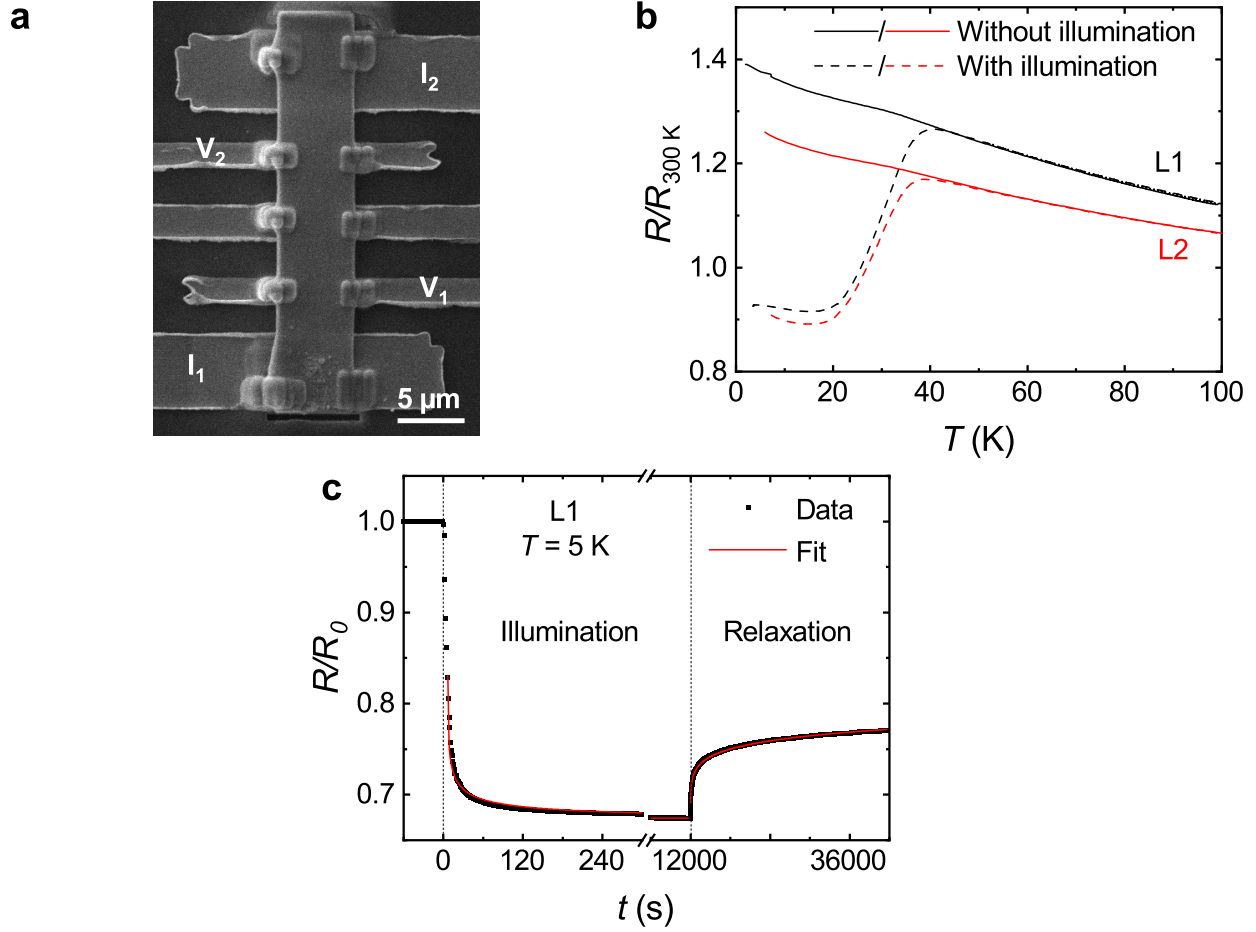
FIG. 3. **Photoconductivity in micro-fabricated $Tl_{1-x}Bi_{1+x}Se_{2-\delta}$ ($x = 0.025$) samples. a**: Scanning electron microscopy image of a typical structure with current ($I_1$ and $I_2$) and voltage ($V_1$ and $V_2$) leads. **b**: Temperature dependence of the resistance, normalized to its value at room temperature, without and with illumination in two samples (L1 and L2). **c**: Time dependence upon illumination at 5 K in sample L1. A stretched-exponential relaxation is observed (red line), with an ultralong time constant of $9 \cdot 10^6$ s estimated for the relaxation process.

14
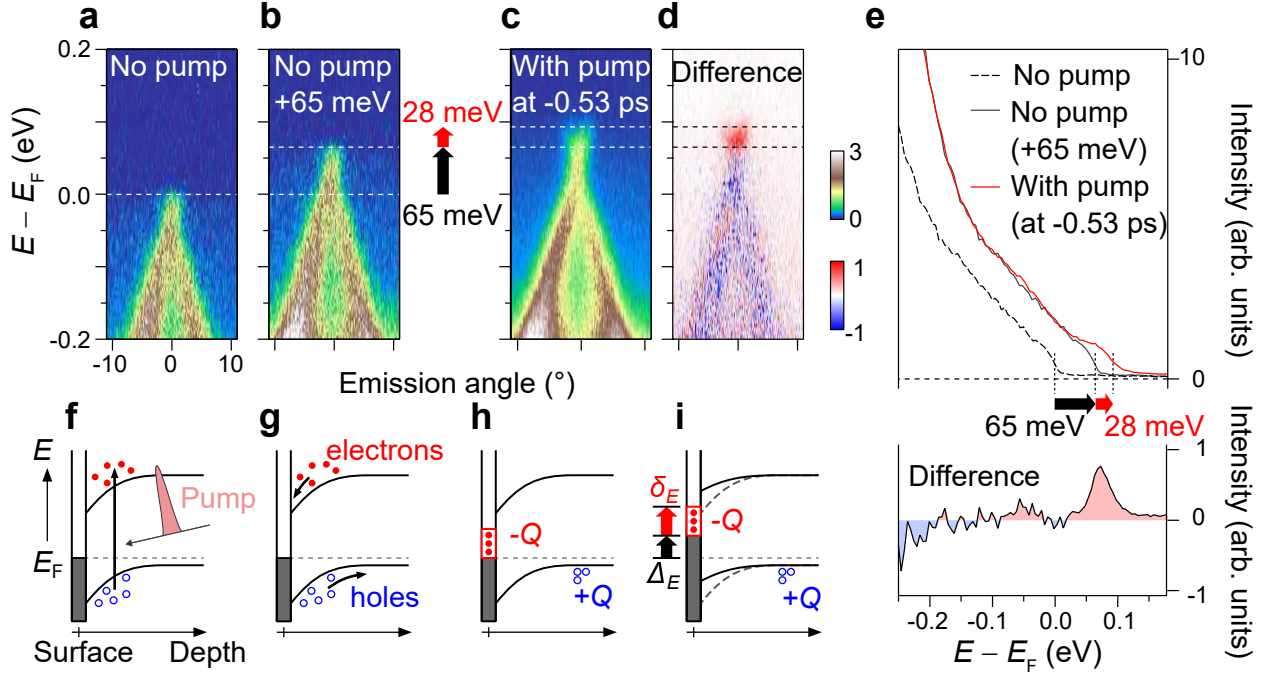
FIG. 4. **Tr-ARPES in Tl$_{1-x}$Bi$_{1+x}$Se$_{2-\delta}$ ($x = 0.025$) at 7 K. a-c**: Dispersion of the surface states around the $\bar{\Gamma}$ point without pump (**a**) and after the longest possible pump-probe delay of $4\mu$s (**c**). The spectrum in **b** corresponds to the one in **a** shifted by $+65$ meV. **d**: Difference between the distributions shown in **b** and **c**. **e**: Angle-integrated energy distribution curves of the spectra shown in **a-c** (top), and difference between the red and solid black curves (bottom). The interval of integration was [-14.5°, 14.5°]. **f-i**: Schematic of the photovoltage generated on the surface of a bulk-insulating topological insulator (see text).

15

##### 349 **Methods**

##### 350 **Sample properties.** The $Tl_{1-x}Bi_{1+x}Se_{2-\delta}$ single crystals ($\delta = 0.28$) used in this study were grown

##### 351 as described in Ref. 24. The bulk band gap is around 300 meV [ 23]. The tuning of the Fermi level

##### 352 by the off-stoichiometry $x$ is confirmed by ARPES and by the dependence of the resistivity on $x$ [ 24,

##### 353 25] (Fig. 1**b**, **c**). Resistivity and current-voltage characteristics give, respectively, an activation energy

##### 354 of around 28 and 25 meV (see Supplementary Information). The depletion depth $W$ is estimated by

##### 355 solving the Poisson equation[40], giving

$$W = \sqrt{\frac{2\epsilon_S}{e^2 n}(E_B - eV - k_B T)}, \tag{1}$$

##### 356 where $\epsilon_S$ is the permittivity of the material, $e$ the elementary charge, $n$ the carrier density, $E_B$ the barrier

##### 357 height, $V$ the applied voltage, $k_B$ the Boltzmann constant, and $T$ the temperature. Using $n = 10^{22}\,\mathrm{m}^{-3}$,

##### 358 the permittivity $\epsilon_S = 21\epsilon_0$ [ 46], and $E_B = 82$ meV obtained from the temperature dependence of

##### 359 the relaxation time (Fig. 2**d**), one finds $W \approx 15$ nm at low temperatures without applied voltage.

##### 360 An estimate of the light penetration depths using the light source is obtained using early studies of

##### 361 TlBiSe$_2$ thin films[47,48]: depending on the growth condition, the light penetration depth at a wavelength

##### 362 $\lambda = 2\,\mu$m (optical response around 1 $\mu$m not reported to the best of our knowledge) varies between 0.16

##### 363 and 1 $\mu$m, which is much larger than the depletion depth, therefore confirming that the light generates

##### 364 bulk excited carriers.

##### 365 **Physical properties.** The resistivity was measured with spot-welded or silver-paint contacts using 10 or

##### 366 25 $\mu$m diameter gold wires. Similar results were observed in different samples and with different con-

##### 367 tact configurations, highlighting the robustness of the results. The samples were obtained by cleaving a

##### 368 larger piece and were typically 0.5-1 mm in length and width, and 50-200 $\mu$m in thickness. The mea-

##### 369 surements were performed down to 2 K, in part in a Physical Property Measurement System (PPMS)

##### 370 from Quantum Design Inc. using either the standard resistivity option or the ac-resistance bridge option

##### 371 for the high-current measurements, and in part in an Oxford flow cryostat with a home-made setup. In

##### 372 the latter, a lock-in SR830, and for the current-voltage characteristics, a Keithley source meter 3624B

##### 373 were used. The specific heat was also measured in the PPMS. The magnetization measurements were

##### 374 performed with a SQUID magnetometer from Cryogenics model S700X, the illumination coming from

##### 375 black-body radiation due to the absence of radiation shields.

##### 376 **Study of the photoresponse.** In the PPMS, the sample faces either the bottom of the last radiation

16

buffer or the cap at the top of the sample chamber, depending on whether or not the radiation buffers provided by Quantum Design Inc. were installed. Accordingly, black-body radiation comes either from the temperature of the last buffer or from room temperature. The last buffer of the radiation shield is close to the sample and its temperature is therefore expected to be only slightly higher than that of the sample. In the flow cryostat, the measurements were done with a thermal radiation shield thermally shorted to the sample holder thus having the same temperature as the sample, ensuring a minimum of spurious radiation. The light source is a commercial infrared LED from SHARP GL4800E0000F with a peak emission wavelength of 0.95 $\mu$m, situated typically 2-3 cm above the sample inside the thermal radiation shield. It is controlled with a Keithley current source 2200.

**Memory effect.** The memory effect was measured by cooling down the sample to 2 K under a permanent or shortly applied (typically a few seconds) large dc or ac current (1 to 50 mA). At low temperatures, the excitation was switched off and the resistivity was measured with a low current of 10 $\mu$A upon heating.

**Fabrication of mesoscopic samples.** We used a Quanta 200 3D dual beam system (ThermoFisher Scientific)—a gallium FIB system combined with a scanning electron microscope—to manufacture micrometric samples. Additionally, the system is equipped with micromanipulators from Kleindiek for in-chamber sample transfer.

Following a typical transmission electron microscope sample preparation recipe, a Pt protection layer of about 150 nm thickness was deposited by electron beam induced deposition to protect the near surface region of the sample. The thickness of the protection layer was increased to about 2 $\mu$m by an ion beam induced deposition (IBID) of Pt.

The preparation proceeded by removing bulk material around the protected area with the ion beam, ending up in an about 2 $\mu$m thick sample. It was freed from bulk by undercutting, followed by lifting it out, and welding it to the sample grid. In consecutive milling steps with decreasing ion currents (we used 1 nA and 500 pA for the medium thinning and 100 pA for fine milling) the thickness of the sample was reduced to about 300 nm. In order to reduce the FIB induced damage generated by the previous milling steps at 30 kV ion acceleration voltage, a final cleaning of the sample was done with 5 kV and 30 pA.

The grid with the sample was rotated by $90°$ and loaded together with the measuring platform to the FIB chamber. After removing the remainder of the protection layer, the sample was welded by ion beam induced tungsten deposition to the micromanipulator tip and cut off from the grid. Subsequently, the

17

sample was transported to the measuring platform, consisting of Ti/Au stripes (5 nm/45 nm thick respectively) on a $SiO_2$/Si substrate, and welded by IBID to the substrate, to stabilize the sample over the electrical contacts. The contacts were fabricated by Pt IBID with Trimethylcyclopentadienyl-platinum [$(CH_3)_3CH_3C_5H_4Pt$] as the precursor and the following ion beam parameters: acceleration voltage 30 kV, beam current 50 pA, dwell time 0.2 $\mu$s, and beam overlap 0 %. The connection of the sample to the substrate was cut after contact deposition.

**Time-resolved angle-resolved photoemission spectroscopy.** The tr-ARPES apparatus consisted of a hemispherical analyzer and a mode-locked Ti:sapphire laser delivering 1.48 eV pump and 5.92 eV probe pulses at the repetition rate of 250 kHz, or at the interval of 4 $\mu$s[49]. The energy and time resolutions were 16 meV and 300 fs, respectively. By utilizing a pin hole attached next to the sample, we estimated the spot diameters of the pump and probe beams to be 250 and 85 $\mu$m, respectively, on the sample surface and also checked that the spot of the pump beam on the sample surface did not shift within 5 $\mu$m when the delay stage in the pump beam path was shifted for 600 ps pump-probe delay. The sample was cleaved by peeling off an adhesive tape attached on the sample in the vacuum chamber at the base pressure of $5 \cdot 10^{-11}$ Torr. Measurements were performed at the temperature of 7 K.

## References methods

46. Konorov, P. P., Yafyasov, A. & Bogevolnov, V. *Field Effect in Semiconductor-electrolyte Interfaces: Application to Investigations of Electronic Properties of Semiconductor Surfaces* (Princeton University Press, 2006).

47. Mitsas, C. & Siapkas, D. Phonon and electronic properties of TlBiSe$_2$ thin films. *Solid State Commun.* **83**, 857 (1992).

48. Mitsas, C. L., Polychroniadis, E. K. & Siapkas, D. I. Structural dependence of the optical absorption in TlBiSe$_2$ thin films near the fundamental absorption edge. *Semicond. Science and Technol.* **8**, S356 (1993).

49. Ishida, Y. *et al.* Time-resolved photoemission apparatus achieving sub-20-meV energy resolution and high stability. *Rev. of Sci. Instrum.* **85**, 123904 (2014).

**Authors contributions** G. E. initiated and M. T. lead the study. M. T., G. E., and M. B. performed the transport, magnetic, and specific heat measurements. K. K. and A. K. synthesized and pre-characterized the materials. Y. I. and S. S. performed the time-resolved ARPES measurements. A. S.-T. prepared the micro-structured samples. M. T. and G. E. analysed the data. S. P. supervised the work. M. T., G. E., and S. P. wrote the paper, with inputs from all authors.

**Data availability** The data are available on requests to the corresponding author.

**Competing interests** The authors declare no competing interests.

**Additional information** Supplementary Information is available for this paper. Correspondence and requests for materials should be addressed to M. T. (taupin@ifp.tuwien.ac.at) or S. P. (paschen@ifp.tuwien.ac.at).

# Supplementary Information

**CURRENT-VOLTAGE CHARACTERISTICS.**

A topological insulator can be naively modelled as a metal-semiconductor-metal device (the "metal" being the surface and the "semiconductor" the bulk). Charge injection from the metal to the semiconductor is frequently modelled by the relation[40]

$$I = I_0(e^{\frac{qV}{\eta k_{\mathrm{B}} T}} - 1), \tag{2}$$

which captures both thermionic emission and tunnelling processes. Here $I_0$ is the saturation current, $q$ the elementary charge, $V$ the applied voltage, $k_{\mathrm{B}}$ the Boltzmann constant, $T$ the temperature, and $\eta$ an ideality factor[40]. The ohmic regime at low current is taken into account by adding a linear term, giving

$$I = I_0(e^{\frac{qV}{\eta k_{\mathrm{B}} T}} - 1) + V/R, \tag{3}$$

where $R$ is the resistance of the sample. With $q = +e$ (the majority carriers being holes), our current-voltage characteristics can be rather well described by the fit, as seen by the red lines in Extended Data 3**a**. The activation energy $E_{\mathrm{A}}$ can be obtained through $I_0$ as $\ln(I_0/T^2) \propto E_{\mathrm{A}}/k_{\mathrm{B}} T$ or through $\ln R \propto E_{\mathrm{A}}/2 k_{\mathrm{B}} T$ [ 40]. The fact that one obtains similar activation energies in both cases (28 and 25 meV, respectively, see the blue lines in Extended Data 3**b**) indicates that the model captures the situation reasonable well. The ratio of tunnelling to thermionic components is given by the ideality factor $\eta$. Departure from unity indicates that tunnelling becomes the dominant process, as observed in our case when lowering the temperature, as shown in Extended Data 3**c**.

At high currents, charge injection directly into the conduction band occurs, giving an increase of the measured voltage upon illumination (shown by the arrows in Extended Data 3**d**). At low temperatures, the effect of the illumination changes at the threshold current: it is reduced at small currents, and enhanced at large currents. This indicates that the switching is caused by carrier injection into the conduction band.

21

**ANALYSIS OF THE HALL COEFFICIENT UNDER ILLUMINATION.**

Under illumination a new conduction channel opens, namely the region of the sample into which the light penetrates. Thus, a simple two-carrier model[27] is not applicable and an extension is needed. With the following reasonable extra assumptions one can nevertheless extract useful information. We assume that the same amount of electrons and holes is generated by the illumination, that the excited electrons migrate to the surface states (where they have the same mobility as without illumination), and that the excited holes represent the new channel and are thus allowed to have a mobility different from the bulk holes. The observed decrease of the (positive) Hall coefficient and increase of the Hall mobility (Fig. S1**a**, **b**) are then only feasible if these extra holes exhibit an increased mobility. With these two assumptions, at low temperature under illuminations we estimate a surface carrier generation of around $1 \cdot 10^{17}$ m$^{-2}$ (8 times the surface carrier concentration without illumination) and an increase of the hole mobility by a factor $3.5$.

To estimate the weight of the excited electrons/bulk holes in the total conductivity, one assumes that the conductivity of each carrier is given by $\sigma_i = q n_i \mu_i$, with $q$ the elementary charge, designed by the subscript $i$, and $n_i$ and $\mu_i$ the corresponding carrier concentration and mobility respectively. At 10 K without illumination, it is $\sigma_e/(\sigma_h + \sigma_e) \approx 10$ %, and under illumination, $\sigma_e/(\sigma_h + \sigma_e) \approx$ 24 % under illumination, an increase by a factor 2.4.

22
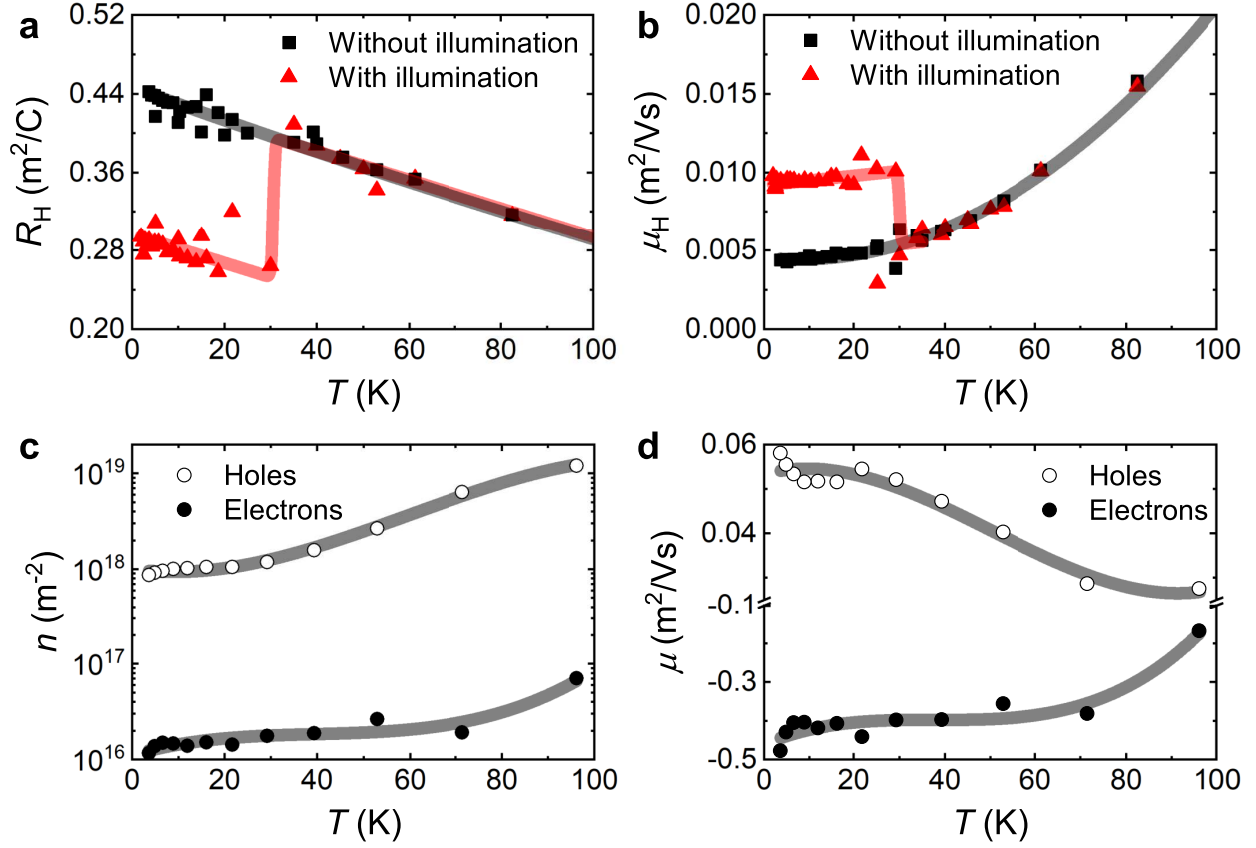
# Extended Data



Extended Data 1. **Photoresponse of the Hall coefficient and the Hall mobility. a**, **b**: Linear-response Hall coefficient $R_H$ and Hall mobility $\mu_H$ without and with illumination (black and red symbols, respectively). Without external excitation, the sheet carrier concentrations and mobilities of the bulk holes and Dirac electrons, estimated using a two-carrier analysis, are given in panels **c** and **d**, respectively. The thick lines are guides to the eyes.
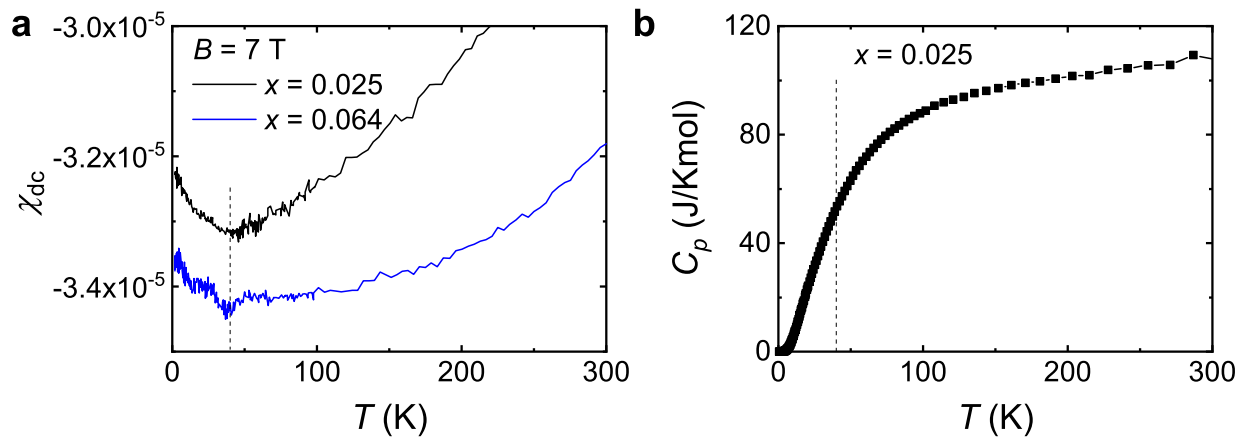
Extended Data 2. **Dc-susceptibility and specific heat. a**: Temperature dependence of the volume magnetic susceptibility $\chi_{\mathrm{dc}}$ in the bulk-insulating ($x = 0.025$) and bulk-metallic ($x = 0.064$) samples. The measurements were performed at a magnetic field of 7 T to enhance the measurement accuracy, but the same behaviour is observed at low fields. **b**: Temperature dependence of the specific heat in the bulk-insulating sample ($x = 0.025$).
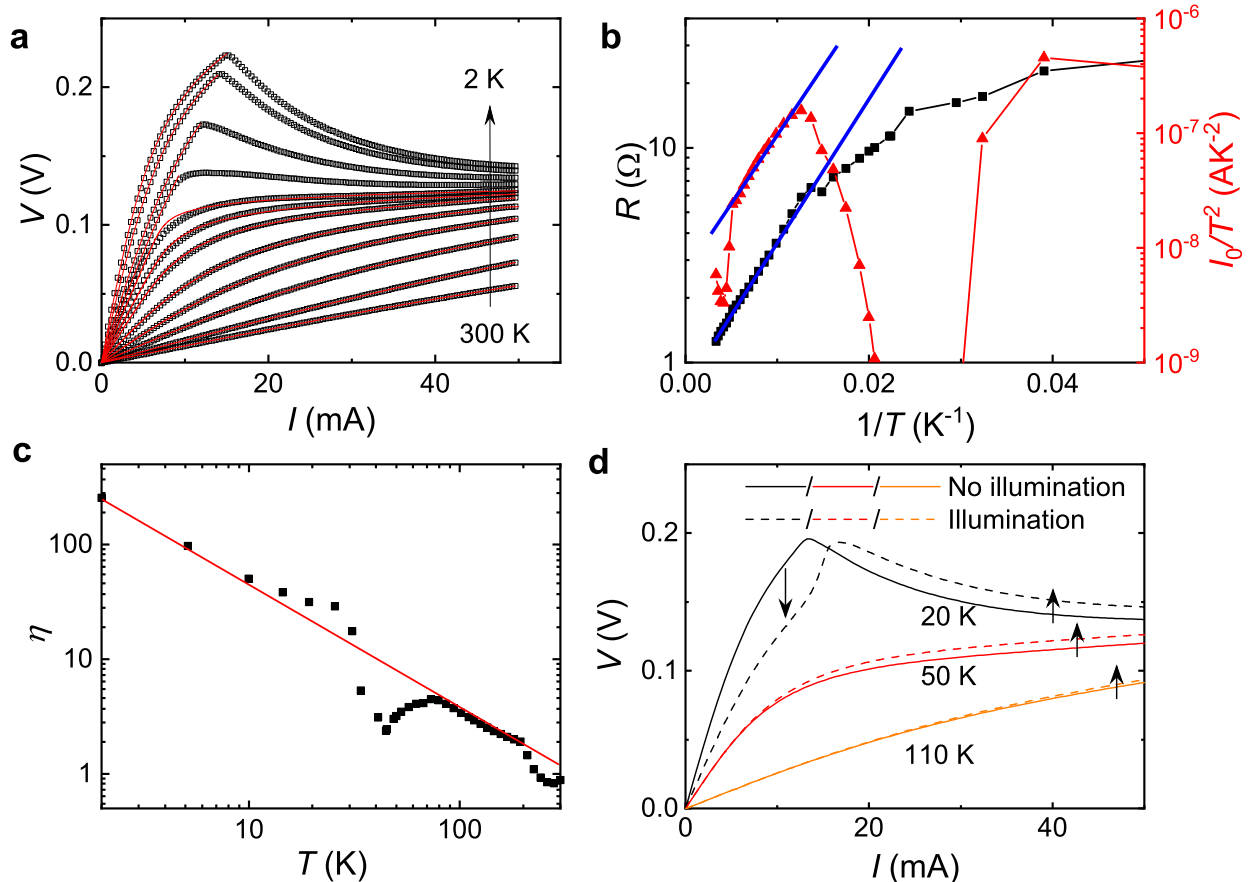
Extended Data 3. **Current-voltage characteristics. a**: Temperature dependence of current-voltage characteristics without illumination (in fact, in our setup, we drive a current through the system and measure the voltage response); they can be described as a metal-semiconductor junction (red lines, see Supplementary Information). **b**: Resistance (in black, left axis) and $I_0/T^2$ (red, right axis, see Supplementary Information) versus $1/T$; the blue lines highlight the range of thermally activated behaviour. **c**: Temperature dependence of the ideality factor $\eta$; the red line is a guide to the eyes. **d**: Photoresponse of the current-voltage characteristics, shown by the arrows. For all measurements, a current of 50 mA was briefly applied to switch the sample into the "low resistance" state (purple triangle of Fig. 2**b**). For temperatures above $T^*$, the characteristics present an increase of voltage under illumination in the whole current range. Below $T^*$, the voltage is reduced upon illumination at small currents, but enhanced at larger currents, after the switching.

25
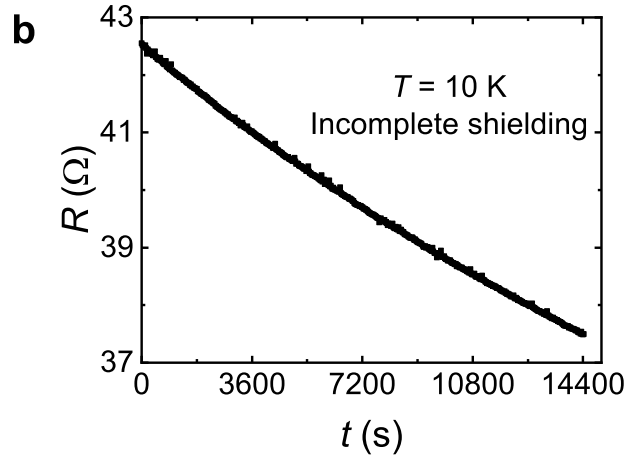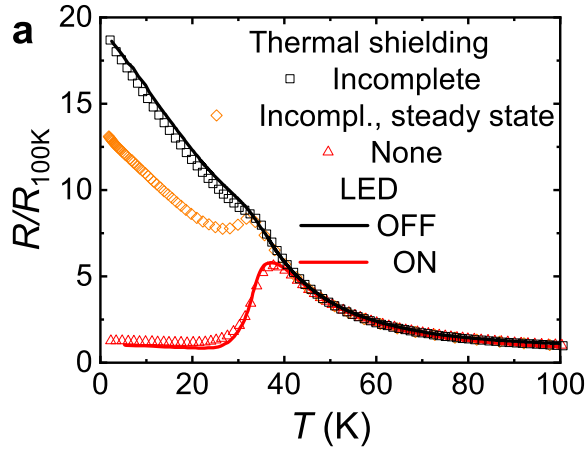
Extended Data 4. **Comparison of illumination with infrared light and with black-body radiation. a**: The measurements with the infrared source (LED) and under black-body radiation from room temperature give similar results (in red). Whereas with the full thermal shielding, the anomaly at $T^*$ is barely visible (black line), a small anomaly appears with incomplete thermal shielding (black points). In this case, the resistance below $T^*$ slowly drifts to lower values (orange points) as shown in panel **b**.
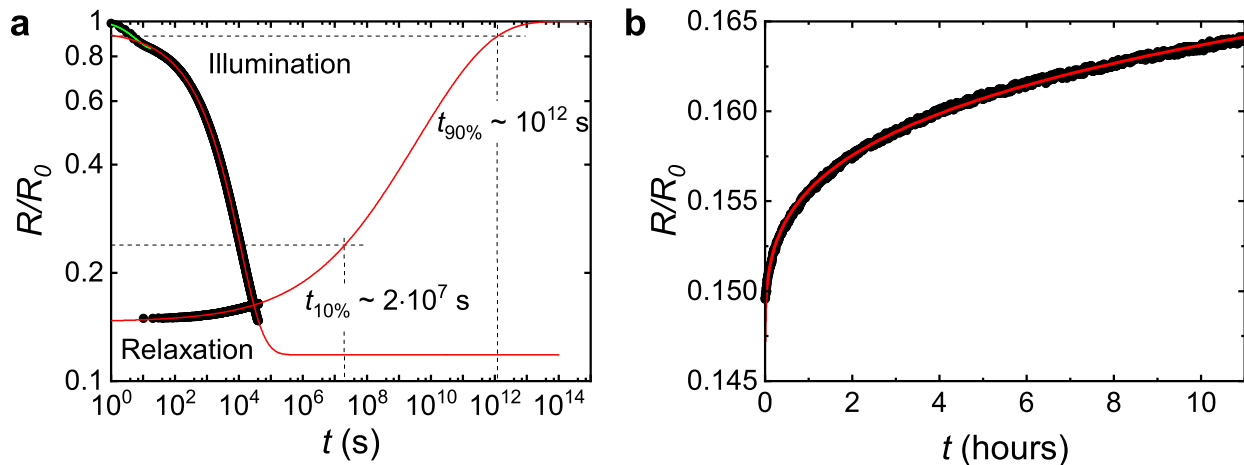
Extended Data 5. **Details on the illumination/relaxation process at 7 K. a**: Normalized resistance during illumination and relaxation (black points). The red lines correspond to fits using stretched exponentials, with the constraint $R_{t\to\infty} = R_0$ for the relaxation process. During illumination, an initial fast exponential decay is observed (green line); we attribute it to overheating when the LED is switched on. **b**: Relaxation process in linear scale with the fit. During relaxation, in 11 hours, the resistance has recovered less than 2% of its initial value.
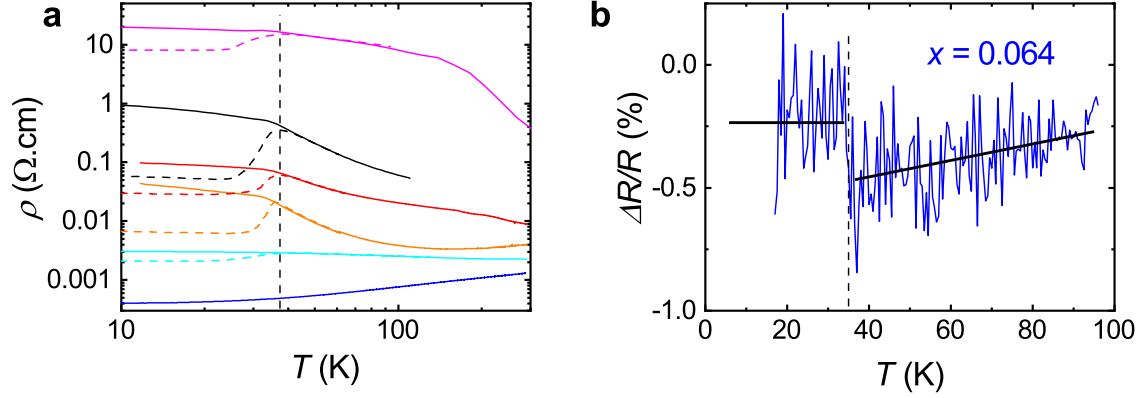
Extended Data 6. **Effect of the illumination on different samples. a**: Resistivity measurements in samples with different off-stoichiometry/doping level, showing the transition from insulating to metallic behavior, without illumination (solid lines) and under illumination (dashed lines). In the case of the bulk metallic sample ($x = 0.064$, in blue), one can still see an anomaly at $T^*$ by looking at the difference of the resistance with and without illumination (panel **b**, note that in this case the illumination is kept on during measurements). Here, one defines $\Delta R/R = (R_{off} - R_{on})/R_{off}$, with $R_{off}$ and $R_{on}$ the resistance without and with illumination respectively. The solid black lines are guides to the eyes.
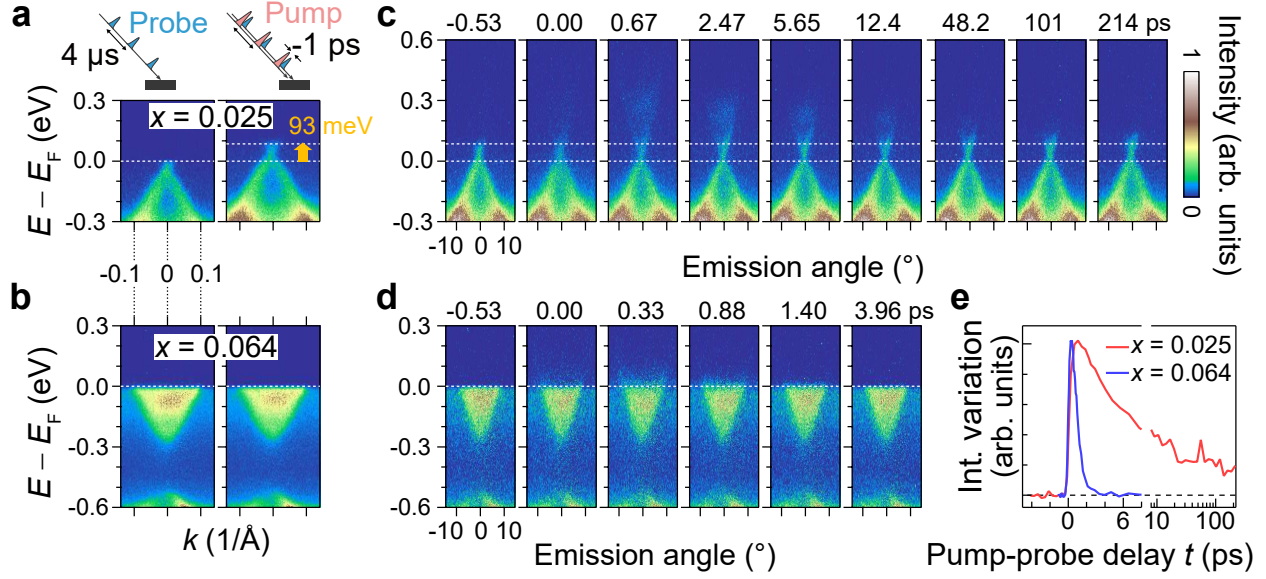
Extended Data 7. **Tr-ARPES for several pump-probe delays at 7 K. a**: Spectra around the $\bar{\Gamma}$ point in the bulk-insulating sample ($x = 0.025$) without (left) and with (right) a pump, at the longest possible pump-probe delay of $4\mu$s, where a surface shift of 93 meV is still present. On top is a sketch of the pump-probe procedure. **b**: Same as **a** in the bulk-metallic sample ($x = 0.064$). **c**: Tr-ARPES spectra at several pump-probe delays (in ps) in the bulk-insulating sample ($x = 0.025$). The negative delay is equivalent to a pump-probe delay slightly shorter than 4 $\mu$s. **d**: Same as **c** in the bulk-metallic sample ($x = 0.064$). **e**: Variation of the intensity as a function of the pump-probe delay in both samples, obtained by subtracting the intensity of the spectrum at 4 $\mu$s (average of 10 images) from the one of each spectrum at various pump-probe delays. The interval of the integration was over the angle [-14.5°, 14.5°] and the energy $E > 0$ (states above the Fermi level).

29